A Modified Limb Correction Algorithm for the Microwave Temperature Sounder of FY Polar-Orbiting Satellites

Xiaoli Qian[ID], Zhengkun Qin[ID], and Juan Li

Abstract— As a new generation of microwave temperature sensor independently developed by China, the microwave temperature sounder-III (MWTS-III) onboard the polar-orbiting satellite FY-3E has 17 channels that provide temperature information from multiple atmospheric layers, making it an indispensable instrument for meteorological research. However, due to the limb effect caused by its cross-track scanning mode, it is impossible to directly observe weather changes using the MWTS-III brightness temperature data. Currently, the limb correction algorithm is an important method to eliminate the limb effect. However, it is difficult to apply existing limb correction methods with fixed parameters due to the newly added channels of MWTS-III. The results of our study show that while the old algorithm can effectively correct the limb effect in most channels of MWTS-III, there are still some limb effects in the corrected results of channels 5–7. On the other hand, the new algorithm can significantly improve the shortcomings of the old method and more accurately eliminate limb effects. In addition, by comparing the limb correction results under different training data, we found that the correction results of the new algorithm have a certain dependence on the training data, and using the same month in the previous year can achieve better correction results. Finally, it has been proved to be applicable to all channels of MWTS-II onboard FY-3D. Specially, the new algorithm can improve the shortcomings of the old algorithm in correcting the limb effect for MWTS-II channel 7, including the lower average brightness temperature at the orbit edge, discontinuous spatial distribution of brightness temperature, and the existence of abnormally low values.

Index Terms— Fengyun meteorological satellites, limb correction, limb effect, microwave temperature sounder (MWTS), polar-orbiting satellite.

I. INTRODUCTION

SATELLITE data has now become the predominant component of meteorological observation data due to its distinctive characteristics, including high spatio-temporal resolution and extensive coverage. Following the launch of the Television and Infrared Observation Satellite-N (TIROS-N) series by the United States in 1978, a number of polar-orbiting meteorological satellites carrying microwave temperature sounders (MWTSs) have been launched globally. During the early development phase of meteorological satellites, the microwave sounding unit (MSU) on polar-orbiting satellites had only four channels for detecting atmospheric temperature profiles. The MSU was replaced by the advanced MSU (AMSU) after the successful launch of NOAA-15 in July 1998. The AMSU Unit A (AMSU-A) has 11 additional channels, which allow for more effective detection of the temperature profile characteristics in different atmospheric layers [1]. The polar-orbiting meteorological satellites launched by the United States and Europe carry similar MWTSs, providing global observation data with high spatio-temporal resolution, which play a vital role in improving numerical weather forecasting. Among various satellite data, the assimilation of polar-orbiting satellite MWTS data has been an essential source for improving the forecast skill [2], [3].

The MWTSs onboard China's polar-orbiting meteorological satellites have undergone independent development. From the first-generation MWTS (MWTS-I) carried by FY-3A/B in May 2008 to MWTS-III carried by the latest polar-orbiting meteorological satellite FY-3E, it has undergone three generations of updates. According to the evaluation results, the instrument performance of MWTS-III is comparable to that of the latest Advanced Technology Microwave Sounder (ATMS) of the United States [4].

Apart from being applied in data assimilation, the MWTS from polar-orbiting satellites can also ensure a reliable time series of upper atmospheric temperature for studying long-term climate trends in the upper atmosphere where traditional radiosonde measurements are lacking [5], [6]. The NOAA series of polar-orbiting satellites provided the earliest microwave data for the research and detection of trends in global temperatures related to climate change. By combining the channels with similar frequencies between MSU and its next-generation AMSU-A, meteorologists have established a long-term satellite dataset. Currently, the MSU/AMSU fusion datasets used for climate research are primarily from Remote Sensing Systems (RSSs), University of Alabama in Huntsville (UAH), and NOAAs Environmental Satellite and Data Information Service (NESDIS) [1], [7], [8].

Xiaoli Qian and Zhengkun Qin are with the Joint Center of Data Assimilation for Research and Application, Nanjing University of Information Science and Technology, Nanjing 210044, China (e-mail: 202211010020@nuist.edu.cn; qzk_0@nuist.deu.cn).

Juan Li is with the Earth System Modeling and Prediction Centre and the State Key Laboratory of Severe Weather, Institute of Meteorological, China Meteorological Administration, Beijing 100081, China (e-mail: lj@cma.gov.cn).

However, due to the cross-track scanning mode, the brightness temperature is not only affected by atmospheric temperature, but also by the scan angle. Therefore, it is necessary to effectively eliminate the impact of scan angle before the application of satellite data [9]. The processing methods for brightness temperature variations caused by scan angle depend on the application method of satellite data. The application modes of satellite data can be roughly divided into three categories based on their usage: assimilation, retrieval, and direct use. In assimilation applications, radiative transfer models are often employed as observation operators for satellite data [10], [11], to simulate brightness temperature based on the atmospheric profile information of the background field. Complex radiative transfer models can reasonably simulate changes in brightness temperatures caused by different scanning angles. In retrieval applications, by using different optimization algorithms, the atmospheric temperature and humidity profiles, and other surface meteorological variables can be retrieved based on brightness temperature [12], [13], [14]. By introducing scan angle as a predictor, many retrieval algorithms can also reasonably account for the impact of scan angles. In the direct-use applications, satellite brightness temperature data can be used to describe the spatial structure of typhoons [15], [16], or is used for the climate change-related research [1], [17], [18], [19], [20], [21]. In such cases, it is necessary to develop independent limb correction algorithms. Otherwise, the brightness temperature differences of several tens of degrees caused by limb effects for different fields of view (FOVs) may obscure weather and climate change information.

The MWTS-III has 98 FOVs sampled per scan line in a stepped-scan fashion, with each separated by $1.36°$. The angular range of an MWTS-III scan is $±66.09°$ relative to the nadir. The instrument observes radiances at different scan angles in different FOVs. A larger scan angle, that is, farther away from the nadir, usually indicates a longer optical path, which leads to a shifting of the weighting function peak to higher levels than that at nadir. This phenomenon of brightness temperature varying with the scan angle is known as the "limb effect" [22]. For the 23.8-GHz window channel, the angle-dependent measurement can result in a brightness temperature difference of up to 30 K between the nadir and the maximum scan angle; while for atmospheric temperature sounding channels (53–58 GHz), the difference reaches as much as 10 K [15].

For the channels with maximum weighting functions in the troposphere where temperature decreases with increasing altitude, the limb effect causes colder brightness temperature at the orbit edge as the observed brightness temperature decreases as the scan angle increases. On the contrary, for channels with maximum weighting functions in the stratosphere where temperature increases with increasing altitude, observed brightness temperature increases as the scan angle increases, resulting in warmer brightness temperature at the orbit edge. The cooling and warming effects at the orbit edge caused by the limb effect are much greater in magnitude than the temperature changes induced by weather systems, thereby hindering the direct identification of weather signals from the spatial distribution of brightness temperature at each MWTS-III channel. This restricts the direct application of microwave temperature data in weather and climate research.

NOAA has substantial expertise in the limb correction at fixed viewing angles. The traditional TIROS Operational Vertical Sounder (TOVS) and Advanced TOVS (ATOVS) detection data have been corrected by NOAA before being applied in climate research [23], [24]. The limb correction algorithm was initially developed for the TOVS channels [22] and later extended to the ATOVS data (NOAA 15, 16, 18, and 19) [25], [26]. Zhang et al. [15] applied the algorithm proposed by Goldberg et al. [23] to the ATMS observation data. Tian et al. [16] also directly applied this algorithm to the FY3D/MWTS-II observation data, and revealed the weather signals by comparing the spatial distributions of brightness temperature before and after limb correction.

To enable the direct application of MWTS-III brightness temperature data in weather and climate research, it is necessary to correct the limb effect caused by its cross-track scanning mode. However, the addition of multiple new channels in MWTS-III makes it impossible to directly use the existing limb correction algorithm. The limb correction algorithm proposed by Goldberg et al. [23] corrects the observed brightness temperature from different scan angles to the brightness temperature at the same altitude level as the nadir by utilizing the temperature gradients between the target channel and its adjacent channels. Yet, due to the varying amplitudes of temperature variations in different atmospheric layers and the differences in the vertical ranges of observation channels, the associated channels vary with the target channels. Existing limb correction studies [15], [16] mostly relied on empirical selection of associated channels based on the settings determined by Goldberg et al. [23]. However, with the continuous improvement of instruments, the lack of objective criteria for selecting associated channels becomes evident when channel parameters are adjusted or new channels are introduced.

The channel parameter settings of MWTS-III onboard FY-3E differ somewhat from those of AMSU-A, with an obvious difference in the number of FOVs within each scan line. AMSU-A has only 30 FOVs, while MWTS-III has 98 FOVs. Furthermore, the polarization modes of the channels with same frequency in the two instruments are opposite, except the channels at 50.3, 52.8, and 54.94 GHz, which have the same polarization mode. More importantly, there are certain differences in the number and frequency of channels between the two instruments. Compared with AMSU-A, MWTS-III has removed the 89-GHz channel and added the 51.76, $53.246 ± 0.08$, and $53.948 ± 0.081$ GHz channels to supplement temperature detection at the near-surface and the levels of 4 and 6 km above the surface in the troposphere, respectively. Therefore, targeted limb correction algorithms need to be developed due to the obvious differences in instrument parameters between the MWTS-III and AMSU-A. In this study, FY-3E/MWTS-III data provided by the National Satellite Meteorological Center was utilized to verify the effectiveness of Goldberg's algorithm in correcting the limb effect for MWTS-III data. On this basis, a relatively objective method for associated channel selection was developed to establish a new universal

limb correction algorithm. Hereafter, the algorithm proposed by Goldberg et al. [23] is referred to as the old algorithm, and the improved algorithm in this study is referred to as the new algorithm.

The remainder of this article is organized as follows. Section II provides a detailed introduction to the FY-3E/MWTS-III data, which serves as the data foundation. The old limb correction algorithm is also introduced. Section III analyzes the effectiveness of the old algorithm applied to MWTS-III. Section IV introduces the new limb correction algorithm. In Section V, a comparison is made between the new and old algorithms. In Section VI, the data independence validation of the new algorithm was conducted. In Section VII, the new algorithm is applied to FY-3D/MWTS-II and compared with previous results. Finally, the main conclusions are presented in Section VIII.

II. DATASETS AND METHODS

A. FY-3E/MWTS-III Data

The MWTS-III is the new generation MWTS carried on the first civil satellite FY-3E in a dawn–dusk orbit launched by China on July 5, 2021. Compared with MWTS-II, MWTS-III has been substantially improved with respect to channel number, spatial resolution, and swath width. On the basis of MWTS-II, four channels with different frequencies have been added, and the spatial resolution has been improved to 16 km. In addition, the swath width has also been increased from 2250 to 2700 km, greatly improving the observation coverage [4].

Specifically, the MWTS-III has added the 23.8-GHz channel to enhance the measurement of total column water vapor, the 31.4-GHz channel as a window channel to improve the measurement of total water vapor, and the 53.246 ± 0.08 and 53.948 ± 0.081 GHz channels to supplement temperature detection within the levels of 4 and 6 km above the surface in the troposphere, respectively. Compared with MWTS-II, MWTS-III has remarkable improvements in the sensitivity and calibration accuracy [27], [28]. Table I reveals significant differences in channel number, frequency, and polarization mode between MWTS-III and AMSU-A. Fig. 1 illustrates the vertical distribution of the weighting functions for each channel of MWTS-III. The weighting functions mainly peak at the surface for channels 1–4, whereas the weighting functions for channels 5–17 peak at different heights, providing the ability to detect the characteristics of temperature at various heights. Among them, channel 17 has the highest weighting function peak, reaching about 2 hPa.

B. Limb Correction Algorithm

Wark [22] proposed a limb correction algorithm that utilizes the linear relationship between the observed brightness temperature of the target channel at nadir and the observed brightness temperature of the associated channels to correct the limb effect at given scan angles. Goldberg et al. [23] inherited and improved the algorithm, proposing a limb correction algorithm using a combined physical and statistical approach. This algorithm uses the physical coefficients as a constraint
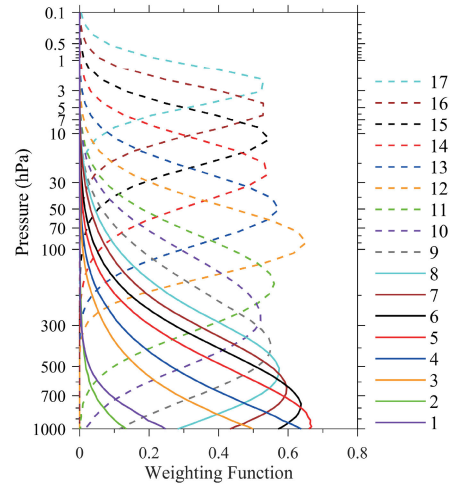

Fig. 1. Weighting functions of MWTS-III. The atmospheric profile comes from the U.S. standard atmosphere. The rapid radiative transfer model adopts the radiative transfer for the TIROS TOVS model version 12.

TABLE I
PARAMETER SPECIFICATIONS OF EACH CHANNEL FROM THE THIRD GENERATION MWTS (MWTS-III) AND AMSU-A

Central Frequency (GHz)	MWTS-III		AMSU-A	
	Channel	Polarization	Channel	Polarization
23.8	1	H	1	V
31.4	2	H	2	V
50.3	3	V	3	V
51.76	4	V	/	/
52.8	5	V	4	V
53.246±0.08	6	V	/	/
53.596±0.115	7	V	5	H
53.948±0.081	8	V	/	/
54.40	9	V	6	H
54.94	10	V	7	V
55.50	11	V	8	H
57.290344(fo)	12	V	9	H
fo±0.217	13	V	10	H
fo±0.3222±0.048	14	V	11	H
fo±0.3222±0.022	15	V	12	H
fo±0.3222±0.010	16	V	13	H
fo±0.3222±0.0045	17	V	14	H
89.00	/	/	15	V

in the statistical model proposed by Wark [22], and follows a constrained least squares procedure to obtain the optimal solution to the statistical model. By using the temperature gradient information of the associated channels with the target channel, the observed brightness temperature at different scan angles is corrected to the brightness temperature information at the same altitude as the nadir.

In the training set of this algorithm, the predictor is the mean brightness temperature anomaly within a 2° latitudinal band at the selected channel of each beam position. In contrast to the Wark's algorithm that uses the mean brightness temperature over a 2° latitudinal band, this algorithm uses the deviations of the mean brightness temperature over latitudinal bands from the global mean for regression analysis, which can reflect brightness temperature variations in different latitudinal bands more accurately [13]. The number of predictors depends on the selection of the associated channels in the correction, which usually are the two channels adjacent to

TABLE II
SELECTION OF ASSOCIATED CHANNELS FOR THE LIMB CORRECTION IN
EACH MWTS-III CHANNEL

Frequency(GHz)	Channel	Associated channels
23.8	1	1,2
31.4	2	1,2
50.3	3	3,4,5
51.76	4	3,4,5
52.8	5	4,5,6
53.246±0.08	6	5,6,7
53.596±0.115	7	6,7,8
53.948±0.081	8	7,8,9
54.40	9	8,9,10
54.94	10	9,10
55.50	11	11,12,13
57.29 (fo)	12	12,13
fo±0.217	13	12,13,14
fo±0.322±0.048	14	13,14,15
fo±0.322±0.022	15	14,15
fo±0.322±0.01	16	14,15,16
fo±0.322±0.0045	17	16,17

Fig. 2. (a) Average brightness temperature of MWTS-III channel 7 at every scan position in every 2° latitudinal band. The data is sourced from July 2022. (b) Relationship between the average brightness temperature of channel 7 at the subsatellite point and the average brightness temperature anomaly of (left) channel 6 and (right) channel 8 for each 2° latitudinal band of MWTS-III. Different colors indicate different FOVs.

the target channel. Since the peaks of the weighting functions of adjacent channels are on both sides of the target channel, there is a good linear relationship in the observed brightness temperature between the associated channels and the target channel, and they are subject to similar interference sources and atmospheric conditions [13]. Table II provides the associated channels for each channel of MWTS-III. The coefficient training equation for limb correction is defined as follows [16]:

$$\overline{T_{k,\text{nadir}}}(j_2) = b_{k,i} + \sum_{k_p=k-1}^{k+1} a_{k_p,i}\left[T_{k_p}(i,j_2) - \overline{T_{k_p}(i)}\right] \quad (1)$$

where $\overline{T_{k,\text{nadir}}}(j_2)$ denotes the mean brightness temperature at target channel k at nadir over the 2° latitudinal band j_2. $T_{k_p}(i, j_2)$ represents the mean brightness temperature over the latitudinal band j_2 at the associated channel k_p of FOV i, while $\overline{T_{k_p}(i)}$ denotes the global mean brightness temperature at the same channel of FOV i. The coefficients $a_{k_p,i}$ and $b_{k,i}$ are the regression coefficients to be trained. These regression coefficients along with $\overline{T_{k_p}(i)}$ will be used to calculate the limb-corrected brightness temperature by the following equation [16]:

$$\overline{T_{k,LC}}(i, j) = b_{k,i} + \sum_{k_p=k-1}^{k+1} a_{k_p,i}\left[T_{k_p}(i,j) - \overline{T_{k_p}(i)}\right] \quad (2)$$

where $\overline{T_{k,LC}}(i, j)$ represents the limb-corrected brightness temperature of channel k at FOV i and scan line j. Limb correction coefficients need to be calculated separately at land and ocean for channels 1–5 that are affected by surface types. However, for channels 6–17, surface types do not need to be distinguished. Fig. 2(a) illustrates the variation of the mean brightness temperature at channel 7 over each 2° latitudinal band with FOV, showing that the mean brightness temperature exhibits a symmetric distribution in each latitudinal band. The gradient of brightness temperature with respect to the FOV attains its maximum in the vicinity of 10°N and then diminishes toward the north (south). Fig. 2(b) shows the relationship between $\overline{T_{k,\text{nadir}}}(j_2)$ of channel 7 and

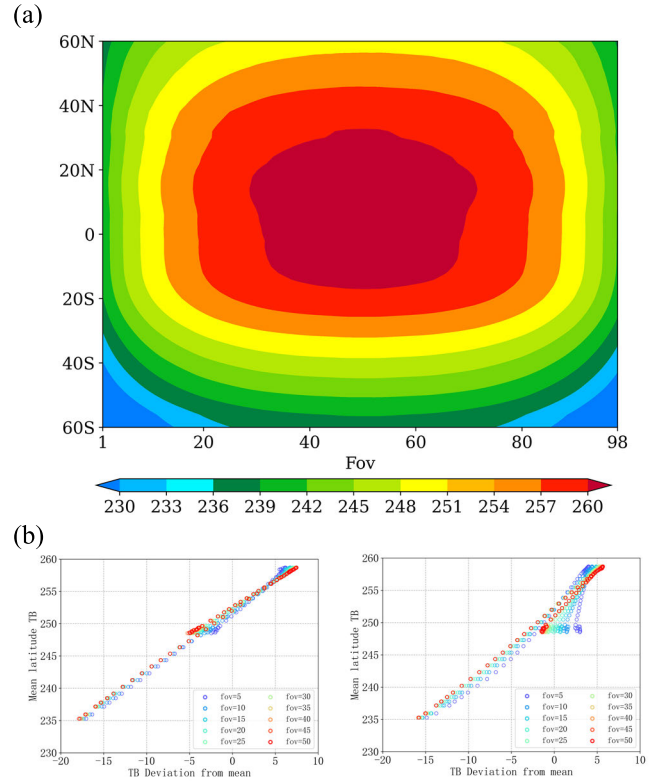the values of $T_{k_p}(i, j_2) - \overline{T_{k_p}(i)}$ at its adjacent channels 6 and 8. Here, $\overline{T_{k,\text{nadir}}}(j_2)$ represents the average brightness temperature of channel 7 at nadir in each latitudinal band, while $T_{k_p}(i, j_2) - \overline{T_{k_p}(i)}$ represents the deviation of the mean brightness temperature in each latitudinal band from the global mean at different FOVs for channels 6 and 8. It indicates that there is a strong linear correlation between these two values, implying that the observed brightness temperatures of channels 6 and 8 can be employed to convert the observed brightness temperature of channel 7 at various scan angles into the brightness temperature at the same altitude level as that of the nadir.

III. BRIGHTNESS TEMPERATURE OF MWTS-III AFTER LIMB CORRECTION WITH THE OLD ALGORITHM

The regression coefficients for limb correction of MWTS-III were trained using the difference between the average brightness temperature of each latitudinal band and the global average brightness temperature in July 2022. Fig. 3 displays a global image of MWTS-III channel 7 observation before and after limb correction on July 10, 2022. Due to the polar orbit overlap, we show the global map with latitude within 60°. Prior to the limb correction, the weighting function of channel 7 was situated in the middle layer of the atmosphere. As the optical path lengthened, the weighting function shifts upward, resulting in a cooling effect at the orbit edge and making it difficult to observe atmospheric temperature features in the
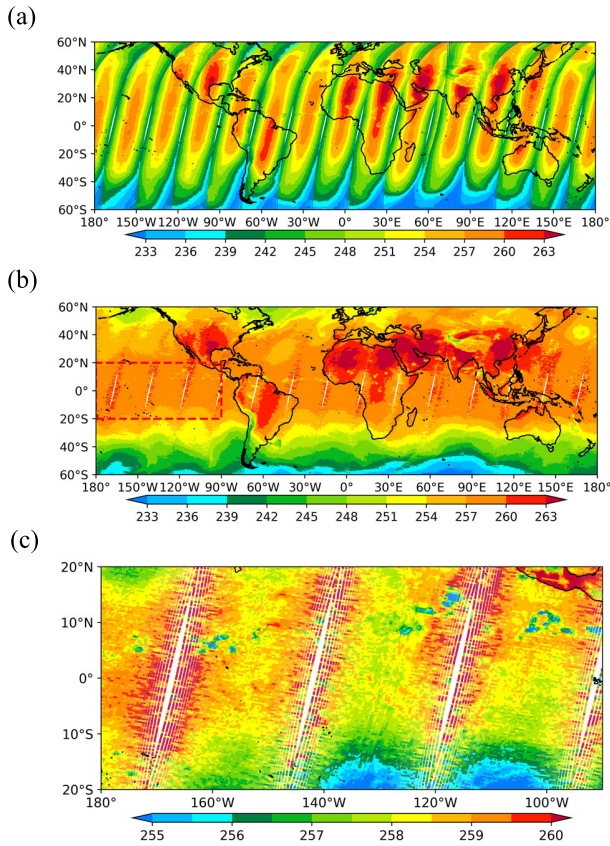
(a)

(b)

(c)

Fig. 3. Spatial distribution of MWTS-III brightness temperature for channel 7 descending orbits on July 10, 2022 (a) before and (b) after limb correction, and (c) smaller subregion in (b) (units: K).
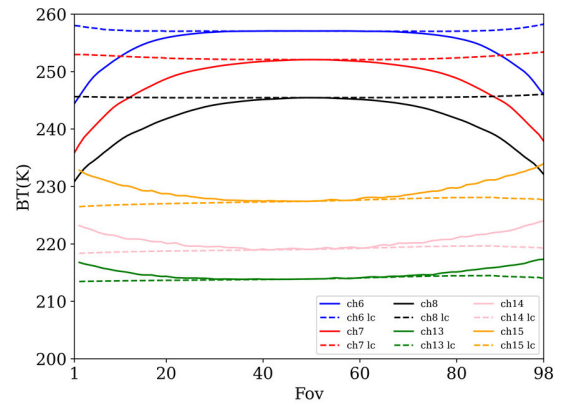

Fig. 4. Variation of average brightness temperature with FOV for different MWTS-III channels before and after limb correction in July 2022. Solid lines represent before correction, and dashed lines represent after correction. Different colors represent different channels.
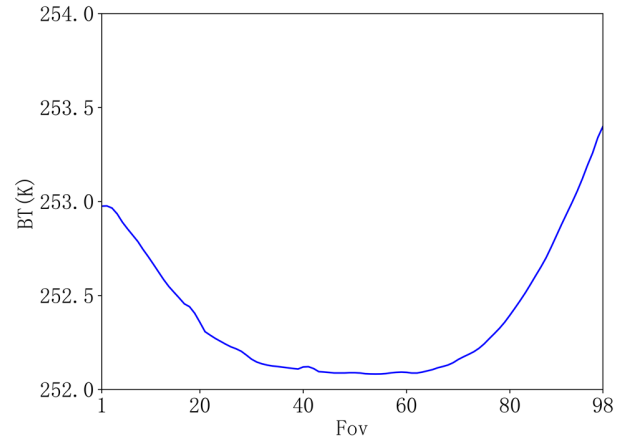

Fig. 5. Variation of monthly average brightness temperature with FOV after limb correction for MWTS-III channel 7 in July 2022.

spatial distribution of brightness temperature [see Fig. 3(a)]. Following correction with the old algorithm, the limb effect of channel 7 was mostly eliminated, allowing for the direct observation of continuous weather variation features in the spatial distribution of brightness temperature [see Fig. 3(b)]. However, many high values occurred after correction in the orbit edge of latitude within 30°. In order to more clearly demonstrate the shortcomings of the old algorithm, the brightness temperature over part of the Pacific region (between 20°S and 20°N) is selected to further clarify the spatial distribution characteristics of the brightness temperature corrected by the old algorithm [see Fig. 3(c)]. It can be seen that although the brightness temperature has good spatial continuity in the global map, in small regions, the corrected brightness temperature at the edge of the orbit is significantly higher than that in similar internal regions of the orbit, indicating that the limb effect has not been completely eliminated.

To better evaluate the effectiveness of the MWTS-III limb correction, Fig. 4 displays the monthly average brightness temperature variation with FOV before and after limb correction for certain weighting functions located in the tropospheric and stratospheric sounding channels in July 2022. Prior to limb correction, the associated channels (channels 6–8) demonstrated a cooling effect at the orbit edge, while the stratospheric channels (channels 13–15) exhibited a warming effect at the orbit edge, primarily due to the opposite temperature variations with altitude in the convection and stratospheric regions. Following limb correction, the phenomenon of bright-

ness temperature variation with FOV was notably improved, indicating that the corrected brightness temperature of each FOV represents the temperature information of the same atmospheric layer at the subsatellite point.

To further clarify the reason for the occurrence of abnormally high-value points at the orbit edge in tropical regions in Fig. 3(b), Fig. 5 presents the brightness temperature variation curve of channel 7 after limb correction with FOV. It is evident from Fig. 5 that the monthly average brightness temperature of channel 7, after limb correction, displays a significant warming effect at the edge. The observed brightness temperature of the FOV at the orbit edge is about 1.5 K higher than the brightness temperature at the subsatellite point. This indicates that the old algorithm resulted in excessive correction at the orbit edge in channel 7.

IV. IMPROVED LIMB CORRECTION ALGORITHM

Goldberg et al. [23] emphasized that the selection of associated channels is crucial in limb correction. Using too many or too few associated channels can lead to inaccurate correction coefficients, which will have a negative impact on the effectiveness of limb correction. Typically, only adjacent channels are considered as associated channels. First, the correlation coefficients in brightness temperature anomalies between adjacent channels and target channel are usually high
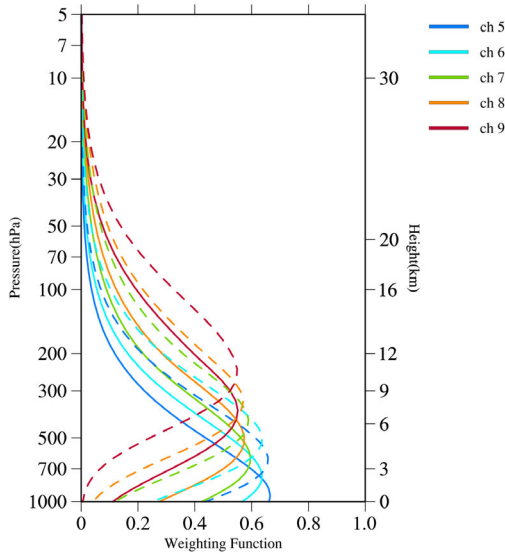
Fig. 6. Weighting functions of the MWTS-III channels 5–9. Solid curves are at nadir, and dashed curves are at a scan angle of 60°.
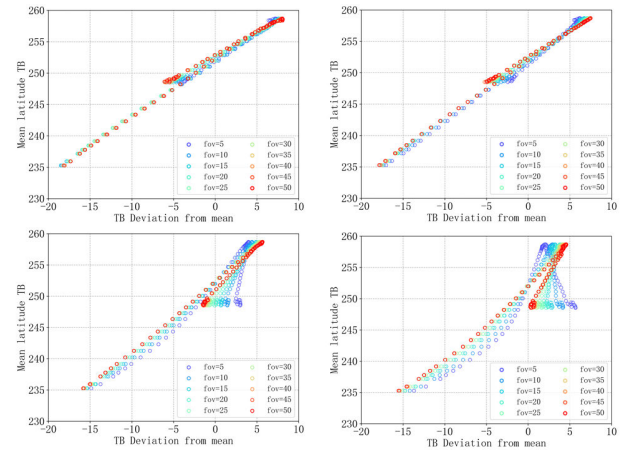

Fig. 7. Relationship between the average brightness temperature of channel 7 at the subsatellite point and the average brightness temperature anomaly of channels 5, 6, 8, and 9 for each 2° latitudinal band of MWTS-III. Different colors represent different FOVs.

because they are close in frequency and are subject to similar interference sources and atmospheric conditions. Second, only using adjacent channels as associated channels can prevent correction errors from accumulating over multiple channels, which will ensure the accuracy of limb correction. Therefore, only the upper and lower adjacent channels are usually selected as associated channels to improve the accuracy of limb correction.

However, the adjustment of channel parameters and the addition of new channels in MWTS-III resulted in over correction of channel 7 brightness temperature at the orbit edge. The over correction may be related to the channel configuration of MWTS-III. For the AMSU-A channel 5 with similar frequency to the MWTS-III channel 7, the frequencies of its two adjacent channels are 52.8 and 54.4 GHz, respectively. While MWTS-III has added two new channels with frequencies of 53.246 ± 0.08 and 53.948 ± 0.081 GHz. Due to the small frequency difference between adjacent channels, the temperature gradient information provided by the associated channels is insufficient, resulting in over correction at the orbit edge. Fig. 6 illustrates the weighting functions of MWTS-III at nadir and orbit edge (with a scan angle of 60°). Compared with AMSU-A, it is apparent that the peak of weighting function of the associated channels selected for limb correction at MWTS-III channel 7 in the old algorithm is very close to the target channel, which cannot provide sufficient information about the temperature gradient. This issue exists at both nadir and the edge of scan. Therefore, selecting the optimal associated channels is crucial for improving the effectiveness of limb correction. Especially for newly added channels, a new objective method for selecting associated channels needs to be established.

In limb correction, associated channels are required to provide information on the variations of temperature gradient with FOV at different altitudes, and the frequencies of the associated channels should be similar to those of the target channel. Hence, this study proposed a relatively objective

method for selecting the associated channels, which is based on the strength of the linear relationships of the upper and lower adjacent two channels with the target channel. The specific steps of this new algorithm are as follows.

First, using one-month observation data of MWTS-III, regression coefficients $a_{k_p,i}$ and $b_{k,i}$ between each associated channel of the target channel in (1) and the residual standard deviation of the linear regression are calculated. The formula for calculating the residual standard deviation of linear regression is as follows:

$$\varepsilon_{k_p}(i) = \text{Std}\left\{ b_{k,i} + a_{k_p,i} \left(T_{k_p}(i, j_2) - \overline{T_{k_p}(i)} \right) - \overline{T_{k,\text{nadir}}}(j_2) \right\} \tag{3}$$

where k represents the target channel, k_p represents the associated channel, i represents the beam position, and j_2 is the index for every 2° latitudinal band.

Second, by calculating the average residual standard deviation $\overline{\varepsilon}$ at all FOVs in the first step, channels with $\overline{\varepsilon} \leq 2$ are defined as associated channels for the target channel. The threshold value 2 is empirically determined by calculating the residual standard deviation ε of the associated channels in the old algorithm.

Third, the associated channels obtained in Step (2) are used to perform limb correction by applying them in (1) and (2).

Taking the MWTS-III channel 7 as an example, the improved limb correction algorithm is introduced. Fig. 7 shows the corresponding relationships between $\overline{T_{k,\text{nadir}}}(j_2)$ of channel 7 and $T_{k_p}(i, j_2) - \overline{T_{k_p}(i)}$ of channels 5, 6, 8, and 9. As the brightness temperature is symmetrically distributed with respect to the FOVs, Fig. 7 only presents the results corresponding to different FOVs to the left of the nadir. It can be seen that there are obvious linear relationships in the brightness temperature between channel 7 and channels 5, 6, 8, and 9. However, the relationship is the strongest in channels 5 and 6 at all scan positions, and in channels 8 and 9 at the scan positions closer to nadir. The relationships of channels 8 and 9 at off-nadir angles are relatively poor.

To determine associated channels more objectively, a quantitative criterion is thus needed during the selection process.
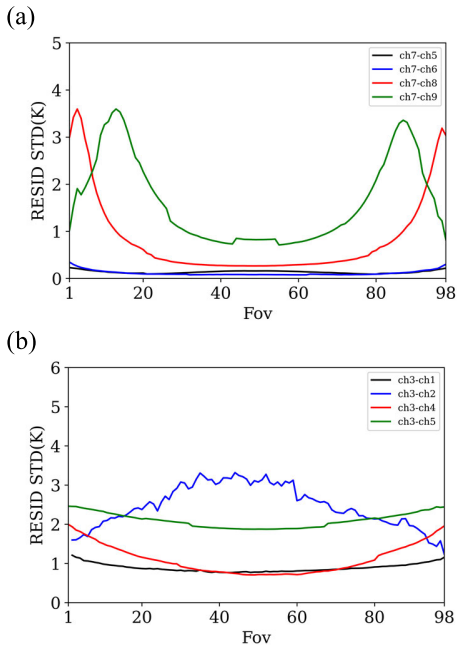
(a)

(b)

Fig. 8. (a) Residual standard deviations between the brightness temperature of MWTS-III channel 7 and its upper and lower two adjacent channels at different FOVs. (b) Same as (a), but for channel 3.
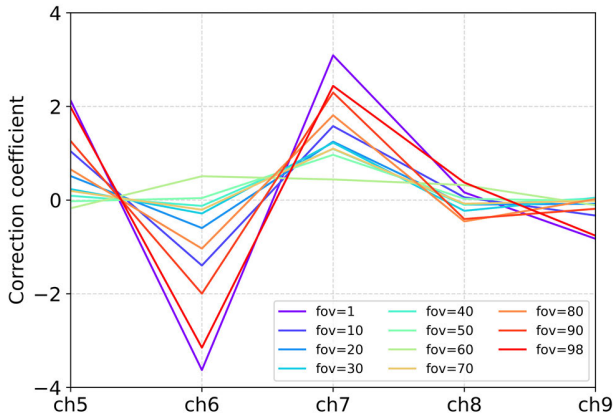

Fig. 9. Limb correction coefficients of MWTS-III channels 5, 6, 8 and 9 for channel 7. Different colors represent different FOVs.

Therefore, this study calculated the residual standard deviation (ε) between the average brightness temperature of channel 7 at nadir and the average brightness temperature anomalies of channels 5, 6, 8, and 9. Fig. 8(a) illustrates those channels 5 and 6 have smaller fitting residuals with channel 7, which remains unchanged with the FOVs. Both channels 8 and 9 have relatively larger fitting residuals at larger off-nadir angles, but the positions where the two channels have larger fitting residuals do not overlap. Channel 8 has larger fitting residuals at FOVs 1–10, while channel 9 has larger fitting residuals at FOVs 10–20. This ensures that during limb correction, there is always one upper-level channel to provide temperature gradient information for channel 7, which will help improve the accuracy of limb correction. Fig. 8(b) shows the result for channel 3, whose adjacent channels have frequencies consistent with those of AMSU-A. It is evident that the ε of channel 3 is much bigger than that of channel 7, especially for adjacent channels 2 and 5.

Channel	Associated channels (Old)	Associated channels (New)
1	1,2	1,3
2	1,2	2,3
3	3,4,5	1,3,4
4	3,4,5	3,4,5,6
5	4,5,6	3,4,5,6,7
6	5,6,7	4,5,6,7,8
7	6,7,8	5,6,7,8,9
8	7,8,9	6,7,8,9
9	8,9,10	7,8,9,10
10	9,10	8,9,10,11,12
11	11,12,13	10,11,12,13
12	12,13	10,11,12,13
13	12,13,14	11,12,13,14,15
14	13,14,15	13,14,15,16
15	14,15	13,14,15,16,17
16	14,15,16	14,15,16,17
17	16,17	15,16,17

To clarify the roles of different associated channels in correcting data from various FOVs, the coefficients for each associated channel used in the channel 7 correction are presented here. Fig. 9 shows that the weights of the associated channels are nearly zero when approaching the nadir, while the weight of channel 7 is close to 1. As the scanning angle increases, channels 6 and 7 have the most significant increase in coefficients, but they change in opposite directions. Channel 5 also experiences an increase in coefficient with scanning angle, but the increase is comparatively smaller.

In contrast, the influence of channels 8 and 9 is relatively small, and the influence of channel 8 is mainly reflected in the middle of the orbit, for example, at the 40th FOV. The coefficient of channel 8 is 0.2. In addition, at the position of large scanning angle (80–90 FOV), the coefficient of channel 8 can also reach −0.2. The influence of channel 9 is mainly reflected in the vicinity of FOV greater than 90, and for the 98th FOV, the coefficient of channel 9 can reach −0.5. These features are consistent with the results in Fig. 7.

For each channel, the averaged residual standard deviation over all FOVs ($\bar{\varepsilon}$) is calculated for the four adjacent channels. Empirically, only channels with the $\bar{\varepsilon}$ less than 2 K can be used as the associated channels, so as to avoid the channel with large fitting error that affects the limb correction. For channel 7, the values of $\bar{\varepsilon}$ for the four adjacent channels 5, 6, 8, and 9 are 0.137, 0.113, 0.826, and 1.63 K, respectively, which are all found to be less than the threshold of 2 K. However, for channel 3, the values of $\bar{\varepsilon}$ for its four adjacent channels 1, 2, 4, and 5 are 0.89, 2.47, 1.1, and 2.1 K, respectively. Therefore, only channels 1 and 4 were selected as the associated channels for limb correction of channel 3.

The selection of associated channels for all MWTS-III channels was examined by analyzing the residual standard deviation. Table III displays the results of the selection using both the new and old algorithms.

V. COMPARISON OF THE NEW AND OLD LIMB CORRECTION ALGORITHMS

The new method can enhance the correction effect of all channels to some extent. However, since high-altitude
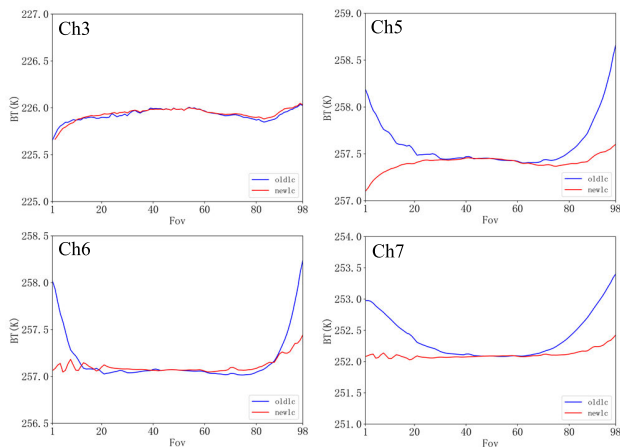
Fig. 10. Variations of monthly average brightness temperature with FOV after limb correction for MWTS-III channels 3 and 5–7 in July 2022. Blue and red lines represent the results of old and new algorithms, respectively.

channels mainly detect stratospheric temperature information, and the temperature vertical gradient in the stratosphere is small, the empirical method of selecting associated channels used in the old method can also achieve good correction results. Although the new correction method can also show improved correction effects, the improvement is relatively small compared to channels 5–7. For low-altitude channels, it is relatively challenging to validate the improvement effect of the correction method since it is significantly affected by weather processes and underlying surface types. Even after correction, the average brightness temperature of low-altitude channels is still difficult to show stable changes along the beam position. Therefore, we will not discuss other channels separately here.

A. Verification of the Correction Effect Over Sea Areas

Fig. 10 illustrates the variation of monthly average brightness temperature with FOV for MWTS-III channels 3 and 5–7 in July 2022. The figure shows that the correction results of the new algorithm vary asymmetrically with the FOV. There are also some small variations in the monthly average brightness temperature after the limb correction of the new algorithm (red curves in Fig. 10). This may be due to the influence of weather systems on the data used to calculate the mean values. The correction results of the old algorithm still exhibit a symmetric distribution with the subsatellite point as the center in channels 5–7. This suggests that the old algorithm still suffers from limb effects. The new algorithm has substantially improved the correction results for channels 5–7, effectively reducing the symmetric distribution of the average brightness temperature with FOV.

To see the difference between the results of limb correction by the two algorithms at the orbit edge more clearly, Fig. 11(a) and (b) depicts the spatial distributions of the brightness temperature after limb correction for MWTS-III channel 7 over the Pacific region on July 10, 2022. It is evident that the difference is more pronounced at the orbit edge, for the result of new algorithm shows much less abnormally larger values than that of the old algorithm, and the brightness temperature
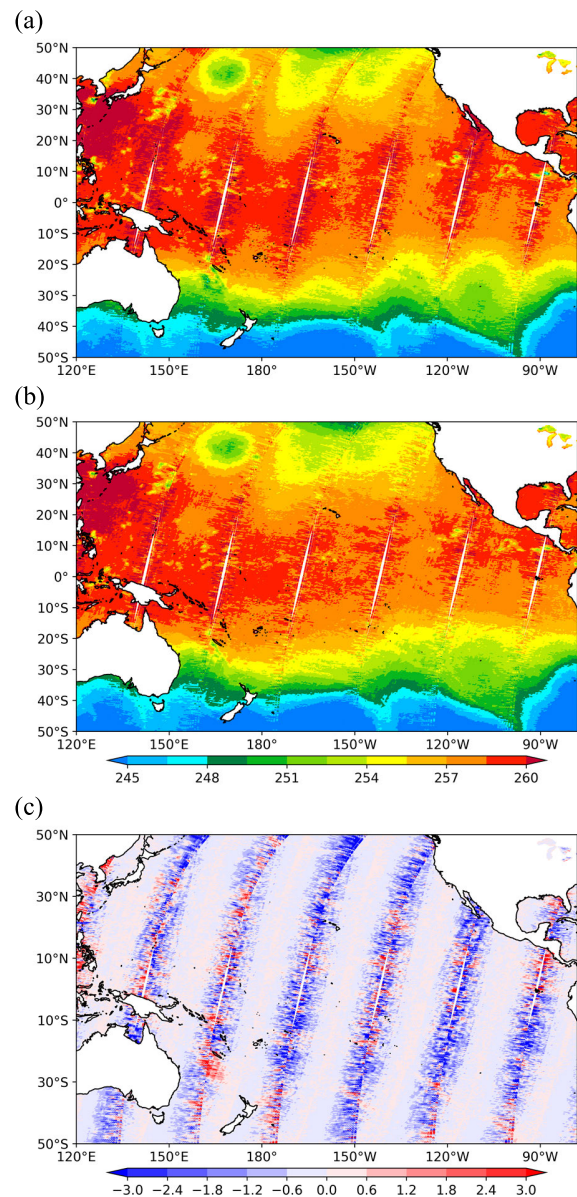

Fig. 11. Spatial distributions of brightness temperature after limb correction for MWTS-III channel 7 over the Pacific Ocean on July 10, 2022 using (a) old algorithm, (b) new algorithm, and (c) their difference (the result of new algorithm minus that of old algorithm).

presents a more continuous distribution in the area near 30°S. Fig. 11(c) shows the spatial distribution of the differences between the results by the two algorithms. It is found that the difference mainly appears at the orbit edge, while the difference near the nadir is less than 0.2 K. Compared with the old algorithm, the brightness temperature obtained from the new algorithm shows negative deviations of about 2–3 K at the orbit edge, and even over 5 K in some area. The consistent negative deviation at the orbit edge indicates that the new algorithm effectively mitigated the abnormally large values at the orbit edge in the mid-latitude region and the unevenly distributed brightness temperature in the high-latitude region obtained by the old algorithm. This demonstrates that the new algorithm can substantially improve the limb correction at the
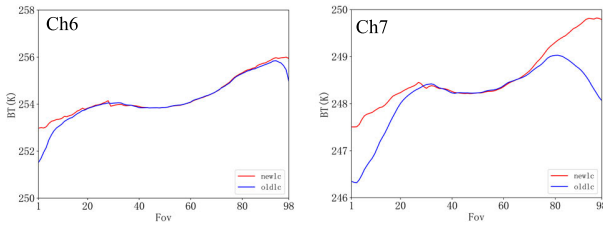
Fig. 12. Variations of monthly average brightness temperature on land with FOV after limb correction for MWTS-III channels 6 and 7 in July 2022. Blue and red lines represent the results of old and new algorithms, respectively.

scan edge by changing the selection of associated channels in the old algorithm.

B. Verification of the Correction Effect Over Land Areas

Due to the impact of the complex and diverse land surface temperature, terrain height, and vegetation type, many channels exhibit more complex variations along the scan line over land areas, which require more considerations for the limb correction over land. During the statistical process of correction coefficient, we excluded the brightness temperature data from high-terrain areas. Nevertheless, the correction coefficients can be used for all land satellite data. Additionally, when calculating the variation curve of monthly average brightness temperature along the beam position, we also removed the brightness temperature from high-terrain areas.

Fig. 12 illustrates the variation of monthly average brightness temperature over land with FOV for MWTS-III channels 6 and 7 in July 2022. The figure indicates that the old algorithm still shows significant symmetric distribution in channels 6 and 7 over land, especially in the orbit-edge areas, suggesting that the correction results still have some limb effects. The new algorithm significantly improves the brightness temperature correction in channels 6 and 7 and effectively eliminates the downward-bending symmetry of the orbit-edge brightness temperature. However, due to the complex underlying surface conditions in land areas, the variation curve of corrected monthly average brightness temperature along the beam position shows a bow shape instead of a straight line seen in oceanic areas. Moreover, combining with Figs. 4, 10(d), and 12(b), we find that in oceanic areas, the old algorithm exhibits significant limb effects due to excessive correction, while in land areas, the old algorithm cannot fully eliminate the limb effects due to insufficient correction.

Similar to Fig. 11, Fig. 13(a) and (b) shows the spatial distributions of corrected brightness temperature for MWTS-III channel 7 over the Eurasian region on July 10, 2022. By comparing the correction results of the two algorithms over land, we find that the new algorithm significantly improves the anomalous low values of the old algorithm near the orbit edge in plain areas, while preserving the low brightness temperature areas observed in high-altitude regions. According to Fig. 13(c), there is a positive bias of 4–5 K near the orbit edge for both algorithms, and in some areas, the positive bias even exceeds 6 K, while there is no significant difference near nadir. Similar to the results in Fig. 11(c), the new algorithm mainly improves the correction effect near the orbit edge, with
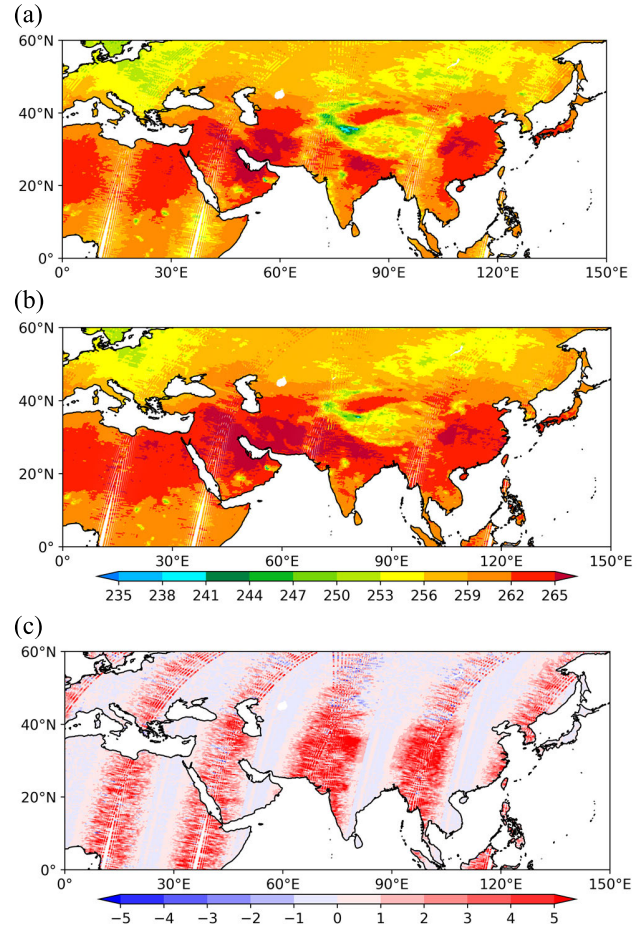

Fig. 13. Spatial distributions of brightness temperature after limb correction for MWTS-III channel 7 over the Eurasian region on July 10, 2022 using (a) old algorithm, (b) new algorithm, and (c) their difference (the result of new algorithm minus that of old algorithm).

negative biases over ocean areas and positive biases over land areas.

VI. DATA-INDEPENDENT VALIDATION OF THE NEW ALGORITHM

To verify the dependency of the new algorithm's correction results on the coefficient training data, we conduct an independence validation study. The correction coefficients were trained separately with data during May 1–31, 2023, June 1–30, 2023, and June 1–30, 2022, and then were used to correct the data on June 10, 2022. Fig. 14(a)–(c) depicts the correction results with the three sets of coefficients. In addition, we calculate the difference between the correction results of the other two correction coefficients and the correction results of the correction coefficients in June 2023 [see Fig. 14(d) and (e)]. In order to express concisely, we will use the results in Fig. 14(a)–(c) to represent the correction results of different coefficients in the following text (the same as the captions of Fig. 14). The spatial distributions of the brightness temperature in results of Fig. 14(a) and (b) are nearly identical, but in result of Fig. 14(c), the brightness temperature is noticeably higher than in the other two results, leading to a significant difference in the brightness temperature spatial distribution. By comparing the differences between the results of Fig. 14(b)
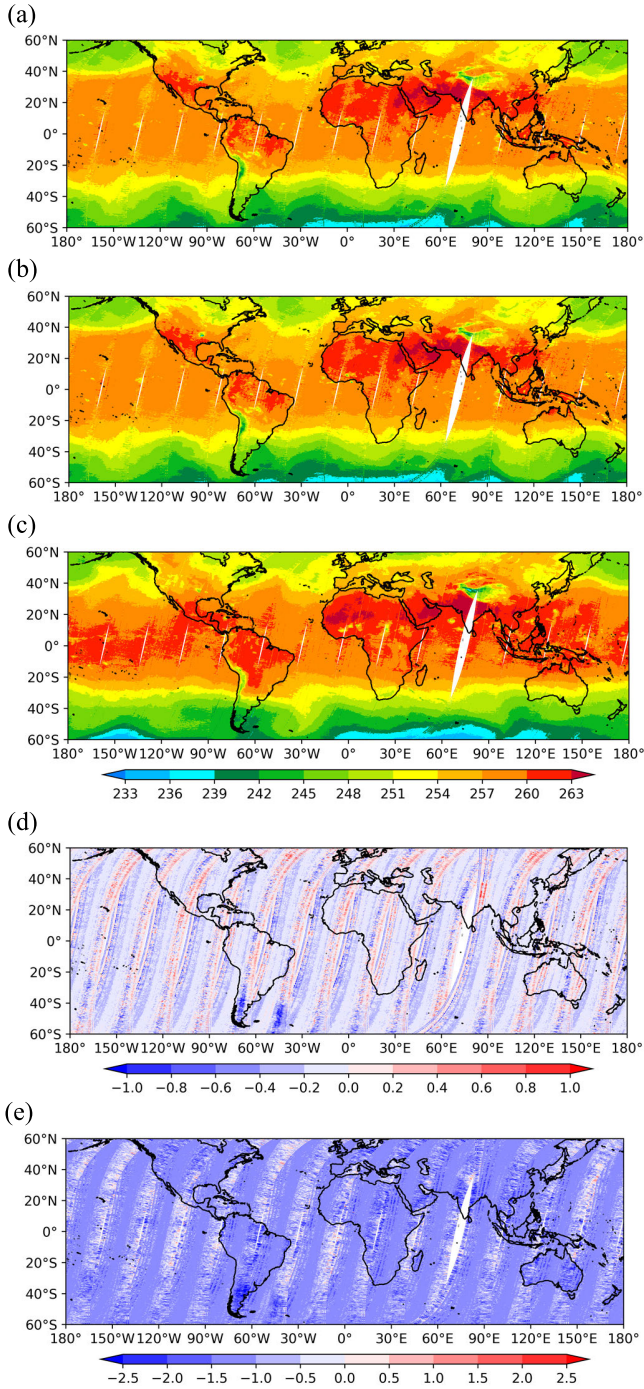
(a)

(b)

(c)

(d)

(e)

Fig. 14. Spatial distributions of brightness temperature after limb correction for MWTS-III channel 7 on June 10, 2023 by using correction coefficients trained in (a) June 2023, (b) June 2022, and (c) May 2023. (d) and (e) Their difference [(d): the result of (b) minus (a); and (e): the result of (c) minus (a)].

and (c) with the result of Fig. 14(a) [see Fig. 14(d) and (e)], we find that the differences between results of Fig. 14(a) and (b) are mainly at the orbit edge (FOV < 3), with the maximum deviation reaching 0.5–1 K (most areas show the deviations less than 0.2 K). However, the difference between the results of Fig. 14(a) and (c) is significantly higher than that between the results of Fig. 14(a) and (b), with an overall deviation of over 1 K and even up to 2 K at the orbit edge. The primary cause of the deviation is that training the correction coefficients requires the monthly average brightness temperature at the

TABLE IV
ASSOCIATED CHANNELS SELECTED IN THE TWO LIMB CORRECTION
ALGORITHMS FOR MWTS-II

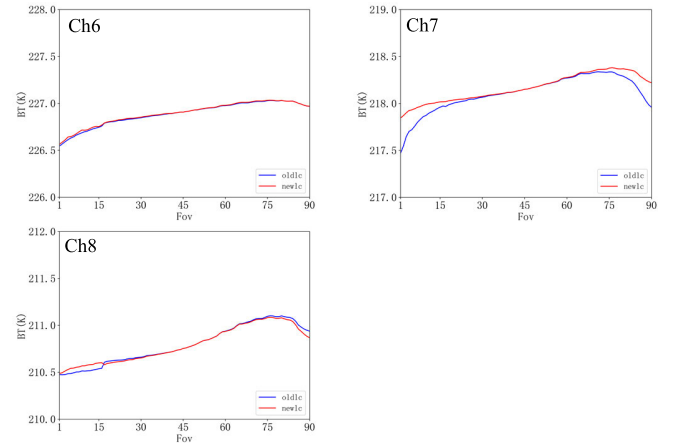| Channel	Frequency(GHz)	Predictor channels(Old)	Predictor channels(New)
1	50.3	1,2,3	1,2
2	51.76	1,2,3	1,2,3,4
3	52.8	2,3,4	1,2,3,4
4	53.596	3,4,5	2,3,4,6
5	54.4	4,5,6	3,4,5,6
6	54.94	5,6	4,5,6,7,8
7	55.5	7,8,9	6,7,8,9
8	57.29 (fo)	8,9	6,7,8,9,10
9	fo±0.217	8,9,10	7,8,9,10,11
10	fo±0.322±0.048	9,10,11	9,10,11,12
11	fo±0.322±0.022	10,11	9,10,11,12,13
12	fo±0.322±0.01	10,11,12	10,11,12,13
13	fo±0.322±0.0045	12,13	11,12,13

Fig. 15. Variations of monthly average brightness temperature with FOV after limb correction for MWTS-II channels 6–8 in July 2022. Blue and red lines represent the results of old and new algorithms, respectively.

subsatellite point. If there is significant interannual variation, the correction coefficients will differ greatly, leading to incorrect correction results. Therefore, in practical applications, we can train the correction coefficients using observation data from the corresponding month of the previous year to obtain accurate correction coefficients.

VII. EXPERIMENT ON THE LIMB CORRECTION OF MWTS-II USING THE NEW ALGORITHM

In order to further verify the reliability of this new algorithm, we applied it to FY-3D/MWTS-II. Table IV shows the associated channels selected in the new and old algorithms, where the associated channels in the old algorithm were kept consistent with that of Tian et al. [16]. The experiment was conducted using MWTS-II observation data in July 2022.

Fig. 15 illustrates the variations of monthly average brightness temperature with FOV after limb correction by the two algorithms for MWTS-II in July 2022. As for the average temperature, the two algorithms only showed obvious differences at channel 7 of MWTS-II. Though the phenomenon of colder brightness temperature at the orbit edge still existed after limb correction by both algorithms, the new algorithm achieved a remarkable improvement with the maximum reduction reaching about 0.3 K.
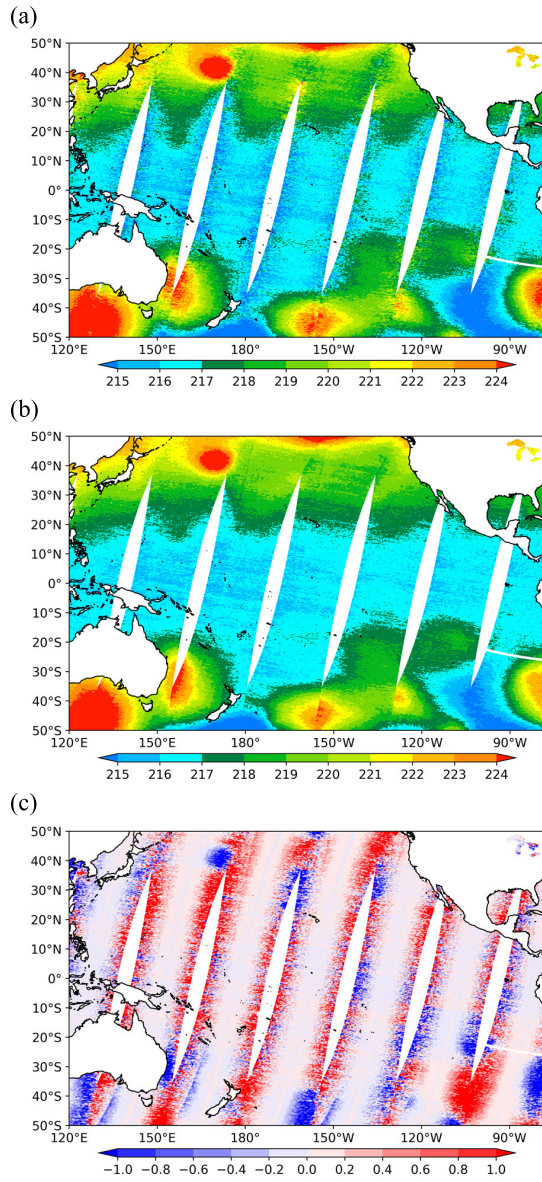
(a)

(b)

(c)

Fig. 16. Spatial distributions of brightness temperature after limb correction for MWTS-II channel 7 over the Pacific Ocean on July 10, 2022 using (a) old algorithm, (b) new algorithm, and (c) their difference (the result of new algorithm minus that of old algorithm).

Fig. 16(a) and (b) illustrates the spatial distributions of brightness temperature over the Pacific Ocean at channel 7 after limb correction by the two algorithms on July 10, 2022. The figure clearly reveals that obvious smaller values of brightness temperature are found at the orbit edge in the old algorithm, indicating a certain bias in the correction results. In contrast, the new algorithm obtained slightly higher brightness temperature at the orbit edge, indicating a substantial improvement in the colder brightness temperatures with respect to the old algorithm. Furthermore, the brightness temperatures of the new algorithm exhibit a more continuous distribution, indicating a remarkable improvement in the correction effect at the orbit edge.

Fig. 16(c) depicts the difference in the spatial distributions of limb-corrected brightness temperature at channel 7 between the two algorithms. It can be seen that there are mainly obvious

positive deviations of 0.6–1.0 K at the orbit edge, with a maximum deviation reaching up to 3 K. This is consistent with the conclusion that the new algorithm improved the phenomenon of colder brightness temperature at the orbit edge in the old algorithm, as mentioned earlier. Additionally, the new algorithm also improved the problem of discontinuous distribution of extreme values in the correction results of old algorithm. Several areas with obvious negative deviations also appear, which primarily correspond to the extreme-value areas located at the orbit edge. The optimization of the extreme value distribution may be due to the higher ability of the new algorithm in accurately reflecting the influence of air temperature and humidity, which also indicates that there may be a certain degree of inaccuracy in the old algorithm.

VIII. CONCLUSION AND DISCUSSION

As an instrument onboard the world's first civil satellite in a dawn–dusk orbit developed by China, FY-3E/MWTS-III is capable of observing air temperature at different altitudes globally. Its observation data can improve and enrich China's modern meteorological observation system, and also fill the gaps in satellite observations within the 6-h assimilation window. However, due to the limb effect caused by the cross-track scanning mode of MWTS-III, the MWTS-III observation data cannot be used for observing the weather changes directly.

This study utilized FY-3E/MWTS-III observation data in July 2022 to implement limb correction using the algorithm proposed by Goldberg et al. [23]. Based on this algorithm, a new limb correction algorithm was proposed to improve the selection of associated channels and was compared with the old algorithm. Finally, the new algorithm was applied to FY-3D/MWTS-II observation data for further verification.

The results indicate that the old limb correction algorithm can be effectively applied to most channels of MWTS-III. However, for channels 5–7, the old algorithm shows a clear over-correction phenomenon in the monthly average brightness temperature over the ocean as the FOV changed from a temperature decrease at the edge to a temperature increase at the edge. Over land, there is a clear under-correction phenomenon. In contrast, the new algorithm not only maintains good correction effects for most channels but also significantly improves the problems in channels 5–7 of the old algorithm over both ocean and land areas, especially at the orbit edge where the limb effect still exists. The new algorithm optimizes the correction method based on the different characteristics of the ocean and land, which could more accurately eliminate the limb effect and improve the accuracy and reliability of brightness temperature data. In addition, comparing the edge correction results under different training data shows that the correction result of the new algorithm is robust and independent of the training data. Finally, the new algorithm is also applicable to MWTS-II observation data, which improves the issues of lower monthly mean brightness temperature at the orbit edge, discontinuous spatial distribution of brightness temperature, and abnormally low values in the limb correction results for channel 7 by the old algorithm.

In this study, we only conducted the new limb correction algorithm on the MWTS-III and MWTS-II observation data

in July 2022, which may raise concerns about the dependence of the limb correction results on the training data. Sensitivity tests shown here indicate that best results are obtained when seasonal (e.g., monthly) changes are accounted for, and correction coefficients may need to be derived that are temporally varying. To address this issue, we plan to further apply the new correction algorithm to microwave temperature data from additional satellites and from different time periods.

REFERENCES

[1] C. A. Mears and F. J. Wentz, "Construction of the remote sensing systems V3.2 atmospheric temperature records from the MSU and AMSU microwave sounders," *J. Atmos. Ocean. Technol.*, vol. 26, no. 6, pp. 1040–1056, Jun. 2009, doi: 10.1175/2008jtecha1176.1.

[2] J. R. Eyre, "Progress achieved on assimilation of satellite data in numerical weather prediction over the last 30 years," in *Proc. ECMWF Seminar Recent Develop. Satell. Observat. Numer. Weather Predicition*. Reading U.K.: ECMWF Publication, 2007, pp. 1–27.

[3] Y. Bao, J. Xu, A. M. Powell Jr., M. Shao, J. Min, and Y. Pan, "Impacts of AMSU–A, MHS and IASI data assimilation on temperature and humidity forecasts with GSI–WRF over the Western United States," *Atmos. Meas. Techn.*, vol. 8, no. 10, pp. 4231–4242, Oct. 2015.

[4] X. Qian, Z. Qin, J. Li, Y. Han, and G. Liu, "Preliminary evaluation of FY-3E microwave temperature sounder performance based on observation minus simulation," *Remote Sens.*, vol. 14, no. 9, p. 2250, May 2022.

[5] R. W. Spencer and J. R. Christy, "Precise monitoring of global temperature trends from satellites," *Science*, vol. 247, no. 4950, pp. 1558–1562, Mar. 1990.

[6] R. W. Spencer and J. R. Christy, "Precision and radiosonde validation of satellite gridpoint temperature anomalies. Part II: A tropospheric retrieval and trends during 1979–90," *J. Climate*, vol. 5, no. 8, pp. 858–866, Aug. 1992.

[7] J. R. Christy, R. W. Spencer, and W. D. Braswell, "MSU tropospheric temperatures: Dataset construction and radiosonde comparisons," *J. Atmos. Ocean. Technol.*, vol. 17, no. 9, pp. 1153–1170, Sep. 2000.

[8] C.-Z. Zou and W. Wang, "Diurnal drift correction in the NESDIS/STAR MSU/AMSU atmospheric temperature climate data record," *Proc. SPIE*, vol. 7456, Aug. 2009, Art. no. 74560G.

[9] F. Tang and H. Dong, "A review of geolocation error assessment and correction methods for polar-orbiting meteorological satellite data," *Meteorolog. Sci. Technol.*, vol. 47, no. 3, pp. 354–361, 2019.

[10] H. Yong, P. Van Delst, and L. Quanhua. (2006). *User's Guide to the JCSDA Community Radiative Transfer Model*. [Online]. Available: ftp://ftp.emc.ncep.noaa.gov/jscda/CRTM

[11] R. Saunders et al., "An update on the RTTOV fast radiative transfer model (currently at version 12)," *Geosci. Model Develop.*, vol. 11, no. 7, pp. 2717–2737, Jul. 2018.

[12] N. R. Nalli, A. Gambacorta, and Q. Liu, "Validation of atmospheric profile retrievals from the SNPP NOAA Unique combined atmospheric processing system. Part 1: Temperature and moisture," *IEEE Trans. Geosci. Remote Sens.*, vol. 56, no. 1, pp. 180–190, Jan. 2018.

[13] Z. Wan, "New refinements and validation of the collection-6 MODIS land-surface temperature/emissivity product," *Remote Sens. Environ.*, vol. 140, pp. 36–45, Jan. 2014.

[14] M. Owe, R. de Jeu, and T. Holmes, "Multisensor historical climatology of satellite-derived global land surface moisture," *J. Geophys. Res.*, vol. 113, 2008, Art. no. F01002.

[15] K. Zhang et al., "A methodology to adjust ATMS observations for limb effect and its applications," *J. Geophys. Res., Atmos.*, vol. 122, no. 21, p. 347, Nov. 2017, doi: 10.1002/2017JD026820.

[16] X. Tian, X. Zou, and S. Yang, "A limb correction method for the microwave temperature sounder 2 and its applications," *Adv. Atmos. Sci.*, vol. 35, no. 12, pp. 1547–1552, Dec. 2018.

[17] Z. Qin and X. Zou, "Modulation effect of the annual cycle on interdecadal warming trends over the Tibetan Plateau during 1998–2020," *J. Climate*, vol. 36, no. 9, pp. 2917–2931, May 2023, doi: 10.1175/JCLI-D-22-0517.1.

[18] A. C. Maycock et al., "Revisiting the mystery of recent stratospheric temperature trends," *Geophys. Res. Lett.*, vol. 45, no. 18, pp. 9919–9933, Sep. 2018, doi: 10.1029/2018GL078035.

[19] S. Po-Chedley, T. J. Thorsen, and Q. Fu, "Removing diurnal cycle contamination in satellite-derived tropospheric temperatures: Understanding tropical tropospheric trend discrepancies," *J. Climate*, vol. 28, no. 6, pp. 2274–2290, Mar. 2015, doi: 10.1175/JCLI-D-13-00767.1.

[20] J. R. Christy, R. W. Spencer, W. D. Braswell, and R. Junod, "Examination of space-based bulk atmospheric temperatures used in climate research," *Int. J. Remote Sens.*, vol. 39, no. 11, pp. 3580–3607, Jun. 2018, doi: 10.1080/01431161.2018.1444293.

[21] C.-Z. Zou and W. Wang, "Intersatellite calibration of AMSU—A observations for weather and climate applications," *J. Geophys. Res., Atmos.*, vol. 116, Dec. 2011, Art. no. D23113.

[22] D. Q. Wark, "Adjustment of TIROS operational vertical sounder data to a vertical view," NOAA, Washington, DC, USA, Tech. Rep. NESDIS-64, 1993.

[23] M. D. Goldberg, D. S. Crosby, and L. Zhou, "The limb adjustment of AMSU—A observations: Methodology and validation," *J. Appl. Meteorol.*, vol. 40, no. 1, pp. 70–83, Jan. 2001.

[24] A. L. Reale, M. W. Chalfant, T. J. Gardner, and L. W. Casey, "Gardner and TOVS operational sounding upgrades: 1990–1992," U.S. Department of Commerce, NOAA, Washington, DC, USA, Tech. Rep. NESDIS 76, 1994.

[25] A. L. Reale, M. W. Chalfant, A. S. Allegrino, F. H. Tilley, M. P. Ferguson, and M. E. Pettey, "NOAA operational sounding products for ATOVS," U.S. Department of Commerce, NOAA, Washington, DC, USA:, Tech. Rep. NESDIS 107, 2002.

[26] Q. Liu and F. Weng, "Uses of NOAA-16 and -18 satellite measurements for verifying the limb-correction algorithm," *J. Appl. Meteorol. Climatol.*, vol. 46, no. 4, pp. 544–548, Apr. 2007.

[27] P. Zhang et al., "FY-3E: The first operational Meteorological Satellite mission in an early morning orbit," *Adv. Atmos. Sci.*, vol. 39, no. 1, pp. 1–8, Jan. 2022.

[28] J. Mao, Z. Qin, J. Li, G. Liu, and J. Huang, "Comparative analysis of striping noise between FY-3E MWTS-3 and FY-3D MWTS-2," *Remote Sens.*, vol. 15, no. 5, p. 1421, Mar. 2023.

Xiaoli Qian received the M.A. degree in meteorology from the Nanjing University of Information Science and Technology, Nanjing, China, in 2022, where he is currently pursuing the Ph.D. degree in meteorology.

His research interests include climate applications of satellite data and satellite data assimilation.

Zhengkun Qin received the B.S. degree in mathematics and the Ph.D. degree in meteorology from the Nanjing University of Information Science and Technology (NUIST), Nanjing, China, in 2001 and 2007, respectively.

From 2009 to 2014, he was a Visiting Scholar with the Department of Earth, Ocean, and Atmospheric Science, Florida State University, Tallahassee, FL, USA, and the Earth System Science Interdisciplinary Center, University of Maryland at College Park, College Park, MD, USA, in 2016. Since 2014, he has been a Full Professor with the Joint Center of Data Assimilation for Research and Application, NUIST. His research interests include satellite data assimilation, bias correction, and noise mitigation.

Juan Li is currently the Deputy Director of the Data Assimilation Division, CMA Earth System Modeling and Prediction Centre, Beijing, China. Her research interests include direct assimilation of satellite radiance data and coupled data assimilation.